Clays and Clay Minerals, Vol. 67, No. 4:357–366, 2019

EFFECT OF CALCINATION TEMPERATURE ON THE STRUCTURE OF CHITOSAN-MODIFIED MONTMORILLONITES AND THEIR ADSORPTION OF AFLATOXIN B_1

Chi Lian, Gaofeng Wang, WenQiang Lv, Zhiming Sun*, and Shuilin Zheng

[1]School of Chemical and Environmental Engineering, China University of Mining and Technology (Beijing), Beijing 100083, China

Abstract—Chitosan (CTS) modified montmorillonite (Mnt) composites (CTS-Mnt), which have been widely reported for the adsorption of heavy-metal ions and biological dyes, have not been applied to the field of mycotoxin adsorption. The current study was focused on the preparation of CTS-Mnt by calcination as a mycotoxin adsorbent for the efficient removal of aflatoxin B_1 (AFB_1). The CTS-Mnt samples obtained were characterized using X-ray diffraction (XRD), Fourier-transform infrared spectroscopy (FTIR), scanning electron microscopy (SEM), and nitrogen adsorption/desorption analysis. The CTS-Mnt samples prepared at various calcination temperatures exhibited varying structural configurations, surface hydrophobicities, and texture properties. The results revealed that stable CTS-Mnt speciments, obtained at <350°C, displayed superior adsorption capacity for AFB_1 from a simulated gastrointestinal tract, increasing from 0.51 mg/g of raw Mnt to 4.97 mg/g. With increased calcination temperature, the effect of pH on the adsorption process of AFB_1 becomes negligible. This study demonstrates that the novel CTS-Mnt has tremendous potential as an AFB_1 adsorbent.

Keywords—Adsorption · Aflatoxin B_1 · Chitosan · Montmorillonite

INTRODUCTION

Mycotoxins are highly toxic and carcinogenic metabolites produced by fungi under appropriate conditions, and are prevalent in feed and food products (Ji et al. 2016; del Pilar Monge et al. 2016). Aflatoxin is one of the most common and toxic mycotoxins. Among the aflatoxins, aflatoxin B_1 (AFB_1), which is a polar molecule with dipole moment of 9.5D (Wang et al. 2019), is the most harmful and its structure is shown (Fig. 8). Until now, various methods, including biological, chemical, and physical, have been proposed for the treatment of products contaminated by mycotoxins. However, biological and chemical methods have several limitations such as long treatment periods, high costs, and damage to the structure and nutrients of food, which restrict their wide applications (Jackson & Bullerman, 1999; Çelik et al. 2013). At present, the adsorption technique with advantages of being nontoxic, highly efficient, and cost-efficient is regarded as the best method for detoxifying mycotoxin-contaminated products (Thimm et al. 2001; Zhu & Yao 2014).

Aluminosilicate minerals, including montmorillonite (Mnt) (Abbès et al. 2008; Anjos et al. 2016), zeolite (Marković et al. 2016a, b), halloysite (Zhang et al. 2015), and rectorite (Sun et al. 2018) provide new insights into the employment of natural materials as mycotoxin adsorbents. Montmorillonite, in particular, exhibits good adsorption of specific mycotoxins. Montmorillonite is widely distributed in nature and has the advantages of low price, large specific surface area, and good adsorption ability. It shows no toxic side effects when used as a mycotoxin adsorbent. The adsorption of AFB_1 by Mnt depends mainly on the ion-dipole interactions between the exchangeable cations of Mnt and the negatively charged polar carbonyl functional group of AFB_1 (Abbès et al. 2008; Markovic et al. 2016a). Because Mnt has a small anion exchange capacity (AEC) and the natural cationic counterions only neutralize rather than reverse the surface charge, it has a small anionic adsorption capacity for AFB_1 (Daković et al. 2012). From recent research, replacement of the natural metal counterions with polymeric organic cations, such as octylphenol polyoxyethylene ether (OP-10) (Wang et al. 2018), stearyldimethylbenzylammonium chloride (STAB) (Wang et al. 2017), dodecyl dimethyl betaine (BS-12), or lauramidopropyl betaine (LAB-35) (Wang et al. 2019), reversed the negative surface charge and, thus, showed great improvement in the adsorption of AFB_1. However, these modifiers have adverse environmental effects.

Biopolymer chitosan (CTS) has advantages of natural abundance, non-toxicity, renewability, biocompatibility, and biodegradability; and adsorbs AFB_1 well. (Zhao et al. 2015). However, CTS also has poor selective adsorption, small surface area, and low porosity (Wang & Wang 2008). In order to overcome the weaknesses of raw Mnt, the existing modifiers, and CTS alone, a CTS-Mnt composite was fabricated by immobilizing the CTS on the Mnt surfaces through calcination. The potential of CTS-Mnt as an adsorbent of AFB_1 was assessed by examining its adsorption characteristics for AFB_1 (Fig. 8).

* E-mail address of corresponding author: zhimingsun@cumtb.edu.cn
DOI: 10.1007/s42860-019-00042-z

This paper was originally presented during the World Forum on Industrial Minerals, held in Qing Yang, China, October 2018

MATERIALS AND METHODS

Materials

Montmorillonite with a cation exchange capacity (CEC) of 92.18 meq/100 g used in the present study was obtained from the Inner Mongolia Fuller Mining Development Co. Ltd, Neimenggu Province, China. The main mineral compositions of the Mnt (Table 1) were based on XRD analysis. The Mnt was ground to powder to pass through a 200 mesh sieve. The Mycotoxin aflatoxin B_1 (AFB_1) was provided by Fermentek Co. Ltd., Jerusalem, Israel. The purity of the aflatoxin was determined by High Performance Liquid Chromatography (HPLC) and was >99.5%. Chitosan (BR, deacetylation degree 80.0–95.0%) was obtained from Sinopharm Chemical Reagent Co., Ltd., Beijing, China. Other chemical reagents such as phosphoric acid (BR), sodium phosphate monobasic (BR), disodium phosphate (BR), acetonitrile (GR), and sodium hydroxide acetate (BR) were all purchased from the Beijing Reagent Co. (Beijing, China). Acetonitrile and methyl alcohol were chromatographic grade, and other reagents were analytical grade. All reagents were used as obtained without further purification.

Preparation of CTS-Mnt

The chitosan-modified montmorillonite composites (CTS-Mnt) were fabricated in two steps. Firstly, 4 g of Mnt was dispersed in 100 mL of deionized water and stirred for 0.5 h to obtain a uniform clay-mineral dispersion at room temperature. A stoichiometric amount of CTS (6.6 g) was dissolved in 250 mL of 1% acetic acid solution (V/V) and then introduced slowly to the clay-mineral suspension using a peristaltic pump. The mixtures were stirred for another 24 h in a Kexi magnetic force water bath at 60°C. After stirring, the initial pH of the mixtures was 5.5, they were washed to neutral with deionized water by centrifuging for 10 min at 855.27 ×*g*, and dried in an oven at 60°C for 24 h. In the next procedure, the products obtained were calcined in air from room temperature to 150, 200, 250, 300, 350, 400, 450, or 500°C for 2 h. The heating rate was 5°C/min. After calcination, the calcined samples were ground to <200 mesh to obtain a series of CTS-Mnt, which were labeled as: 150-CTS-Mnt, 200-CTS-Mnt, 250-CTS-Mnt, 300-CTS-Mnt, 350-CTS-Mnt, 400-CTS-Mnt, 450-CTS-Mnt, or 500-CTS-Mnt. The sample without calcination was also tested as a reference, and was labeled as R-CTS-Mnt.

Characterization of CTS-Mnt

The crystal structures of the samples were characterized using a D/MAX 2500 X-ray diffractometer (XRD) manufactured by Rigaku Corporation of Akishima, Japan. The tube voltage was 40 kV, the current was 100 mA, the target was Cu, and the scanning step size was 0.02°2θ. The step speed was 10°/min and the scanning range was 2–80°2θ. The samples were subjected to infrared spectrum analysis using an IS10 infrared spectrometer (FTIR) manufactured by Nicolet of Madison, Wisconsin, USA. The scanning range was 400–4000 cm^{-1}, and the tested samples, which contained ~1.5 mg of CTS-Mnt (or Mnt) and 150 mg of KBr, were prepared as KBr pellets. The specific surface area and pore structure of the samples were characterized by a JW-BK static nitrogen absorber. About 0.3 g of sample was weighed into a quartz tube, heated at 105°C for 1 h, and then tested. The morphological characteristics of the sample surface were characterized using scanning electron microscopy (7500F, JEOL, Akishima, Japan). 10 mg of sample was dispersed in 10 mL of ethanol. Then a small amount of the dispersed mixture was spread on a silicon wafer, and finally tested after drying. The hydrophobic properties of the raw Mnt, R-CTS-Mnt, and CTS-Mnt were inferred from the experimental water content. The instrument used in this experiment was GDW-300 programmable temperature and humidity test chamber (Beijing Youkema Test Equipment Co., Ltd,. Beijing, China), the experiment was operated at a temperature of 20°C and relative humidity of 85%. Before the experiment, all samples were dehydrated in an oven at 105°C for 24 h. The moisture content (%) of the sample was calculated according to formula 1

$$m_a = \frac{m_t - m_0}{m_0} \times 100 \quad (1)$$

where m_a is moisture content, m_0 is the initial weight of the dried sample, and m_t is the weight of the sample at time *t*.

AFB_1 Adsorption Experiments

In the present study, all the adsorption experiments were carried out in an adsorption environment with a pH value of 3.5 or 6.5 adjusted by phosphate buffer and at an ambient temperature of 37°C. Adsorption experiments were performed in a sealed 25 mL polypropylene centrifuge tube. The stock solution of AFB_1 (25 mg/L) was prepared by dissolving a known amount of mycotoxin powder in a chromatographic grade methanol solution. All working solutions of varying concentrations ranging from 1.206 mg/L to 5.674 mg/L were obtained by successive dilution. In a typical batch model, 3 mg of the prepared adsorbent was added to a 10 mL aliquot of a phosphate buffer solution containing AFB_1 at various initial concentrations. The mixture was adsorbed in a constant-temperature oscillating water bath at 134.64×*g* for 120 min. At the end of the adsorption, the supernatant was passed through a 0.22 μm filter membrane, and 1 mL of the filtrate was taken to determine the AFB_1 concentration by HPLC. The experiments in the present study were repeated at least three times independently to ensure the accuracy of the test data.

HPLC analysis was performed using a Shimadzu 2030C (Shimadzu, Kyoto, Japan) with an LC-2030 autosampler quaternary pump, a welchrom 4.6 mm×250 mm XB-C18 column, and a LC-2030 diode array detector. Isocratic elution was carried out using a diode array detector with an excitation wavelength of

Table 1 Mineralogical composition of sample

Compositions	Mnt	Gypsum	Cristobalite	Quartz	Albite
Content (%)	85.5	1.7	1.5	2.4	9.9

https://doi.org/10.1007/s42860-019-00042-z Published online by Cambridge University Press

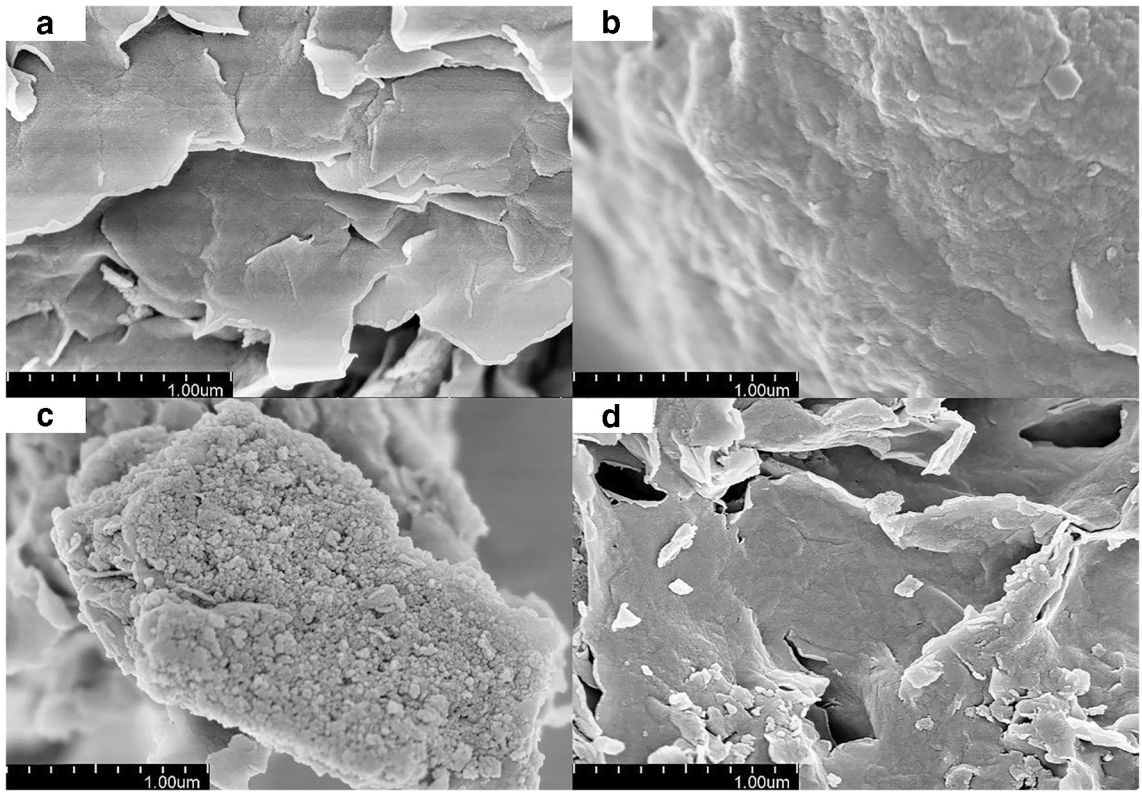

Fig. 1 SEM images of the Mnt (**a**), R-CTS-Mnt (**b**), 350-CTS-Mnt (**c**), and 500-CTS-Mnt (**d**).

360 nm and an emission wavelength of 440 nm. The mobile phase was pumped with water and acetonitrile (50:50, v/v) at a flow rate of 1.0 mL/min. Calibration curves at high standards over the concentration range of the adsorbed samples were obtained and repeated three times. The residual concentration after adsorption equilibrium was obtained from the standard

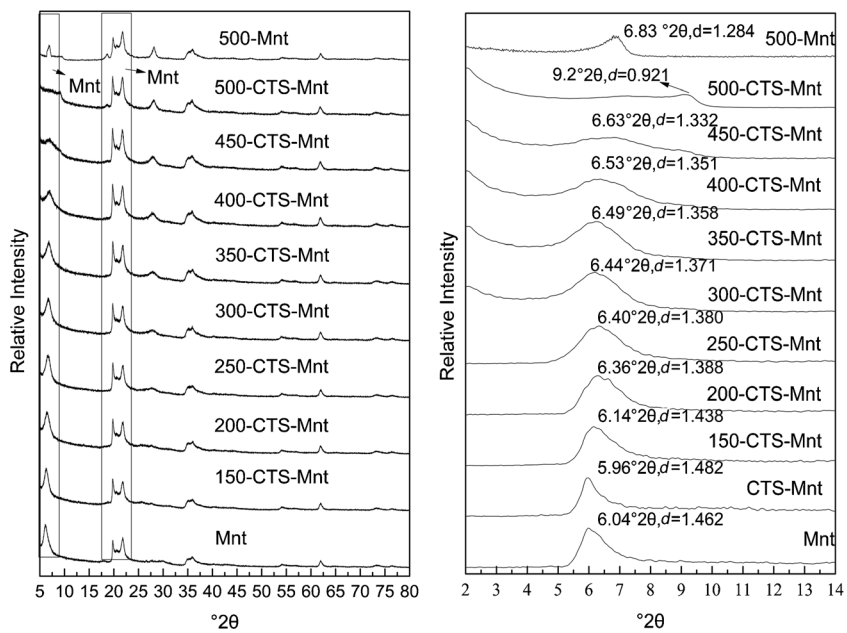

Fig. 2 (**a**) Wide-survey scan XRD patterns of Mnt, R-CTS-Mnt, 500-Mnt, and the heated CTS-Mnt; and (**b**) small angle XRD patterns of Mnt, R-CTS-Mnt, 500-Mnt, and the heated CTS-Mnt.

https://doi.org/10.1007/s42860-019-00042-z Published online by Cambridge University Press

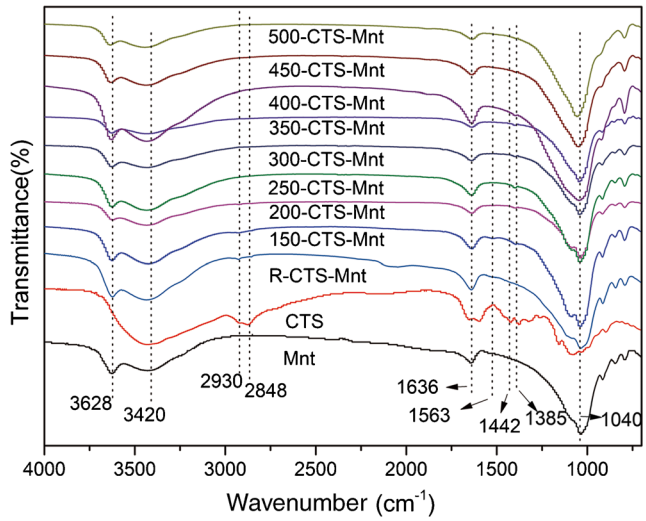

Fig. 3 FTIR images of the raw Mnt, chitosan (CTS), R-CTS-Mnt, and the heated CTS-Mnt.

curve, and the adsorption amount q_t (mg/g^{-1}) was calculated according to formula 2

$$q_t = \frac{(C_0 - C_t)V}{m} \quad (2)$$

where q_t (mg/g) is the adsorbed amount, C_0 (mg/L) represents the initial concentration of AFB_1 in the solution before adsorption, C_t (mg/L) is the equilibrium concentration of AFB_1 in the solution after adsorption, V (L) is the adsorbed volume of AFB_1 and m (g) is the amount of the CTS-Mnt adsorbent.

RESULTS AND DISCUSSION

Characterizations

The calcination temperature has a great influence on the morphology of CTS-Mnt. The SEM images of (a) Mnt, (b) R-CTS-Mnt, (c) 350-CTS-Mnt, and (d) 500-CTS-Mnt (Fig. 1) show that the montmorillonite has a lamellar structure with a smooth surface and completely exposed pore structure (Fig. 1a). For R-CTS-Mnt, the chitosan is wrapped on the surface of the Mnt to form a flocculent shape, and the Mnt pores are blocked (Fig. 1b). When the calcination temperature reached 500°C, 500-CTS-Mnt was similar in morphology to raw Mnt (Fig. 1d). 350-CTS-Mnt (Fig. 1c) has a relatively open structure compared to R-CTS-Mnt and reasonable chitosan loading compared to 500-CTS-Mnt. One could speculate that, on one hand, as the calcination temperature increased from R-CTS-Mnt to 500-CTS-Mnt, the pores of the Mnt were released, which may have a beneficial effect on adsorption for AFB_1. On the other hand, reduced CTS on the surface of Mnt may have led to adverse effects on the adsorption of AFB_1.

The wide survey XRD patterns (a) and small angle XRD patterns (b) of Mnt, R-CTS-Mnt, 500-Mnt, and the heated CTS-Mnt (Fig. 2) revealed that the montmorillonite has a sharp diffraction reflection (001) at 6.04°2θ and a layer spacing of 1.462 nm (Fig. 2b), which is a typical calcium ion-exchanged Mnt (Hu et al. 2016). The interlayer space increased a little from 1.462 nm for the raw Mnt to 1.482 nm for R-CTS-Mnt and the diffraction angle shifted from 6.04°2θ to 5.98°2θ, indicating that a small amount of chitosan had entered the interlayer of the Mnt. In contrast to other studies (Wang et al. 2005, 2014a; Katti et al. 2008), no obvious expansion happened in the interlayer space of Mnt due to the selection of a high degree of deacetylation of chitosan. Compared to intercalation of CTS into the interlayer space of Mnt, the surface immobilization of CTS on the Mnt can retain interlayer exchangeable cations as adsorption sites for AFB_1. With increased calcination temperature, the interlayer spacing reduced to 0.921 nm for 500-CTS-Mnt, and the interlayer space decreased significantly from 1.284 nm for the 500-Mnt to 0.921 nm for 500-CTS-Mnt and the diffraction angle (2θ) shifted from 6.83° to 9.20°(Fig. 2b), indicating that the reduction of the spacing of the montmorillonite layer is mainly due to the carbonization shrinkage of the interlayer chitosan and not just the calcination (Taylor-Lange et al. 2014; Okolo et al. 2015). When the temperature reached 450°C, the diffraction reflection (001) almost disappeared (Fig. 2b). However, the overall structure of Mnt does not change in this process (Fig. 2a).

The infrared absorption spectra of the Mnt, CTS, R-CTS-Mnt, and CTS-Mnt (Fig. 3) showed that the Mnt has absorption peaks at 3628cm^{-1} and 3420 cm^{-1}, which are the stretching vibration and bending vibration peaks of Al-OH in Mnt. The stretching vibration of Si-O-Si in the Mnt appears at 1045 cm^{-1}, which is a characteristic peak of Mnt (Pereira et al. 2013; Wang et al. 2014b; Chen 2016). For the infrared

Table 2 Relative contents (%) of C, N, and O in the R-CTS-Mnt.

Element	Weight percentage	Atomic percentage
C	13.42	16.95
N	7.28	7.88
O	79.30	75.17
Total amount (%)	100.00	100.00

https://doi.org/10.1007/s42860-019-00042-z Published online by Cambridge University Press

Table 3 Relative contents (%) of C, N, and O in the 350-CTS-Mnt.

Element	Weight percentage	Atomic percentage
C	30.65	36.76
N	6.39	6.57
O	62.96	56.67
Total amount (%)	100.00	100.00

absorption spectra of CTS-Mnt, the peak intensity of CTS-Mnt at 3420 cm^{-1} (the -OH and -NH vibration peaks in chitosan) increased at first and then decreased. The CTS-Mnt exhibits the symmetric and antisymmetric stretching vibration peaks of $-CH_2$ at 2930 cm^{-1} and 2848 cm^{-1} (Wang et al. 2007, 2008). However, with the increase of calcination temperature, the symmetry and antisymmetric stretching vibration peaks of $-CH_2$ were gradually weakened. After reaching 400°C, the symmetrical and antisymmetric stretching vibration peaks of $-CH_2$ disappeared completely. The intensity of the band at 1636 cm^{-1} increased at first and then weakened, indicating that the stretching vibration peak of chitosan -CH-CO overlapped the bending vibration peak of the adsorbed water of the Mnt and this caused the increase in intensity. But, as the calcination temperature increased, weakening of the band intensity was caused by the adsorbed water of Mnt and -CH-CO in chitosan decomposing and disappearing. The poorly protonated ammonium group formed by chitosan and acetic acid appeared at 1563 cm^{-1} (Park et al. 2013), indicating that the chitosan may be combined with Mnt in the form of electrostatic adsorption. The characteristic peak of chitosan appeared in the CTS-Mnt at a calcination temperature of 350°C and below, but the characteristic peak of chitosan disappeared completely at a calcination temperature of 400°C and above, illustrating that the basic unit structure of chitosan still exists on Mnt in the range of reasonable calcination temperature. Combined with XRD analysis, stable CTS-Mnt can be obtained at temperatures of <350°C. At the same time, the hydrophobicity of the CTS-Mnt is improved due to the adsorbed water in the CTS-Mnt decreasing, which would be beneficial to the adsorption of AFB_1 by CTS-Mnt.

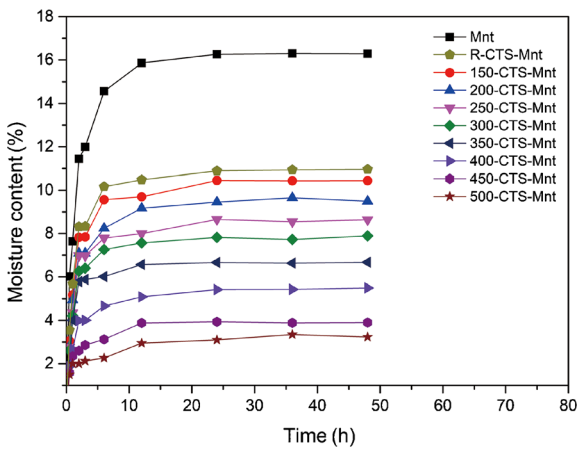

Fig. 4 Moisture adsorption capacities of Mnt, R-CTS-Mnt, and the prepared CTS-Mnt.

The relative contents of C, N, and O in the R-CTS-Mnt and 350-CTS-Mnt (Tables 2 and 3) show that, after calcination, the carbon content of 350-CTS-Mnt increased significantly from 13.42% to 30.65%, which could lead to the enhanced hydrophobicity of CTS-Mnt. Moisture adsorption capacities of the Mnt, R-CTS-Mnt, and CTS-Mnt (Fig. 4) show that as the calcination temperature increased, the adsorption capacity for moisture decreased from 16.3% of raw Mnt to 3.3% of 500-CTS-Mnt, indicating that the CTS-Mnt obtained has better hydrophobicity, which is consistent with the increase in carbon content and the results of the infrared absorption spectra analysis.

The nitrogen adsorption-desorption isotherms of the Mnt and CTS-Mnt (Fig. 5) revealed that the adsorption–desorption isotherm of Mnt exhibits type IV sorption behavior with a H_3 type of hysteresis loop, indicating a characteristic mesoporous material according to the BDDT classification (Brunauer et al. 1940). Compared with the precursor Mnt, the CTS-Mnt also exhibited type IV adsorption behavior. Combined with the pore-size distribution of BJH, the CTS-Mnt is obviously also a mesoporous material. As the calcination temperature increased, the specific areas increased and the BJH pore-size distributions became wider from 150-CTS-Mnt to 500-CTS-Mnt as shown in Table 4, both of which are beneficial to the adsorption of AFB_1.

Effect of calcination temperature

The effect of calcination temperature on the adsorption performance of R-CTS-Mnt and CTS-Mnt to AFB_1 (Fig. 6) was to increase the adsorption efficiency of CTS-Mnt for AFB_1 dramatically from a calcination temperature of 150°C to 350°C. This is expected to result from the increase of carbonization degree of CTS (estimated by the relative contents of carbon atoms and oxygen atoms in Tables 2 and 3). However, the adsorption efficiency decreased slightly with temperature from 350°C to 500°C. Previous studies speculated that chitosan and AFB_1 could combine with polar groups of AFB_1 through polar groups ($-NH_3^+$, $-NH_2^+CO-$) on chitosan (Wang, et al. 2017, 2019). As the calcination temperature increased, the polar functional groups ($-NH_3^+$, $-NH_2^+CO-$) on chitosan decreased gradually and finally disappeared (Fig. 3), which is harmful to the adsorption of AFB_1 by CTS-Mnt.

Isothermal Adsorption of AFB_1

At temperatures of >350°C, chitosan is completely carbonized, as indicated by the infrared spectrum. Therefore, only the adsorption characteristics of CTS-Mnt at calcination temperatures of 350°C or less were studied. Three typical adsorption isotherms were used to study the adsorption characteristics of CTS-Mnt, including the Langmuir, Freundlich, and linear isotherm adsorption models. The Langmuir isotherm adsorption model is an ideal adsorption model that follows a single layer of adsorption and shows that once the adsorbate occurs at a specific location in the adsorbent, no further adsorption occurs. The Freundlich isotherm adsorption model is an empirical adsorption model that is closer to the true adsorption process,

https://doi.org/10.1007/s42860-019-00042-z Published online by Cambridge University Press

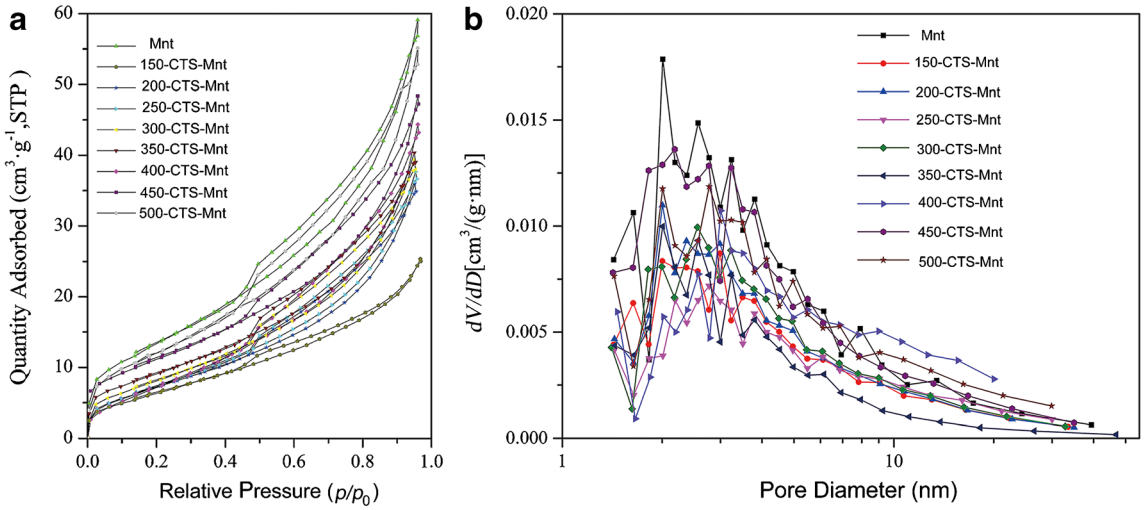

Fig. 5 N_2 adsorption-desorption isotherm and the pore-size distribution plots of the raw Mnt and heated CTS-Mnt.

indicating that multilayer adsorption occurs on heterogeneous surfaces or surfaces of AFB_1 (Xu et al. 2012). According to the results of adsorption isotherms, the initial concentration of AFB_1 and the equilibrium adsorption capacity of the adsorbent were measured at different concentrations, using a linear isotherm adsorption model (formula 3), the Langmuir isotherm adsorption model (formula 4), and the Freundlich isotherm adsorption model (formula 5) to fit the equilibrium data. The results of the fitting are shown in Table 4 and Fig. 7.

$$q_e = K_H C_e \tag{3}$$

$$\frac{C_e}{q_e} = \frac{1}{q_m} C_e + \frac{1}{q_m K_L} \tag{4}$$

$$\ln q_e = \frac{1}{n} \ln C_e + \ln K_F \tag{5}$$

Equations 4 and 5 are linear expressions of the Langmuir and Freundlich isotherm adsorption models, respectively. C_e is the equilibrium concentration of AFB_1 (mg/L) q_e and q_m are the equilibrium adsorption amount and the saturated adsorption amount, respectively (mg/g); K_H is the linear adsorption equilibrium constant; K_L is the Langmuir adsorption equilibrium constant; K_F and $\frac{1}{n}$ are the Freundlich parameters.

The isothermal adsorption curves of CTS-Mnt to AFB_1 fitted by the Langmuir, linear, and Freundlich models (Fig. 7) show that the isothermal adsorption model of CTS-Mnt for AFB_1 is most in line with the Langmuir isotherm adsorption model (R^2>0.99). A previous study showed that the adsorption of AFB_1 by raw Mnt fits the Freundlich isothermal adsorption model (Wang et al. 2018), which indicates that the adsorption sites for AFB_1 in CTS-Mnt and the raw Mnt are different. The saturated adsorption capacity of CTS-Mnt (Table 5) was 3.64 mg/g^{-1} (150-

Table 4 Textural characteristics of the raw Mnt and the heated CTS-Mnt

Samples	S_{BET} (m^2/g)	V_P (cm^3/g)	Pore size (nm)
Mnt	51	0.09	7.18
150-CTS-Mnt	28	0.05	7.90
200-CTS-Mnt	29	0.05	7.89
250-CTS-Mnt	30	0.06	7.81
300-CTS-Mnt	31	0.06	7.75
350-CTS-Mnt	36	0.06	7.51
400-CTS-Mnt	37	0.07	7.40
450-CTS-Mnt	44	0.08	7.31
500-CTS-Mnt	46	0.08	7.21

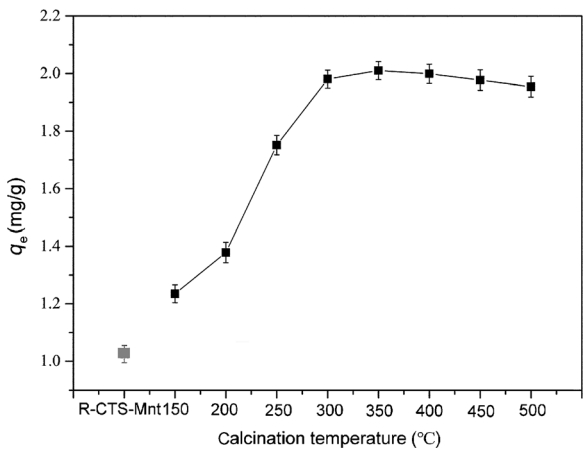

Fig. 6 Effect of calcination temperature on adsorption of AFB_1 by R-CTS-Mnt and CTS-Mnt.

https://doi.org/10.1007/s42860-019-00042-z Published online by Cambridge University Press

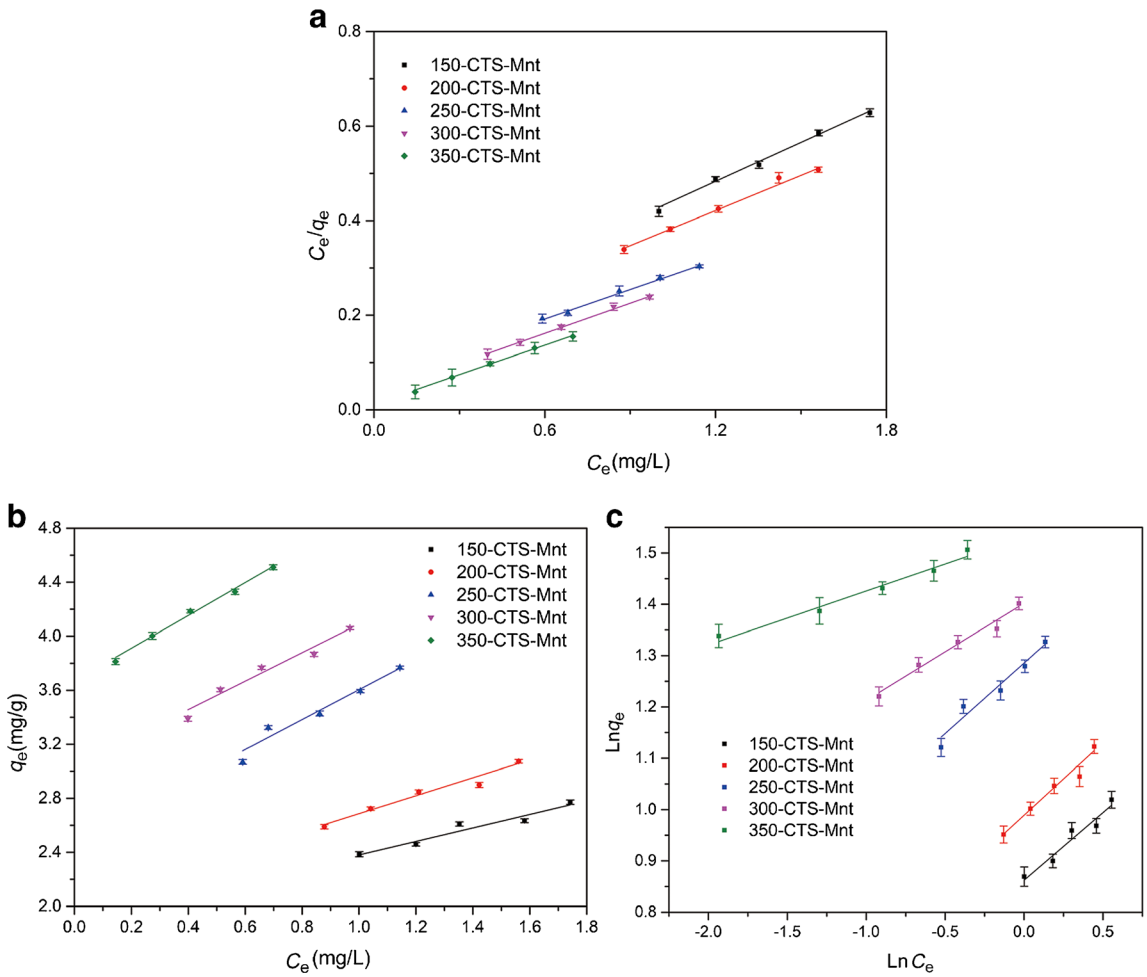

Fig. 7 Isothermal adsorption curves of CTS-Mnt to AFB_1 fitted by (**a**) Langmuir, (**b**) linear, and (**c**) Freundlich models.

CTS-Mnt), 4.03 mg/g^{-1} (200-CTS-Mnt), 4.73 mg/g^{-1} (250-CTS-Mnt), 4.83 mg/g^{-1} (300-CTS-Mnt), and 4.97 mg/g^{-1} (350-CTS-Mnt). The molecular size of an AFB_1 molecule was reported as 1.38 nm^2 (Phillips et al. 1995). The calculated specific surface areas required for CTS-Mnt to become saturated are 15 m^2/g (150-CTS-Mnt), 17 m^2/g (200-CTS-Mnt), 20 m^2/g (250-CTS-Mnt), 20 m^2/g (300-CTS-Mnt), and 21 m^2/g (350-CTS-Mnt). The measured specific surface areas of the CTS-Mnt are 28 m^2/g (150-CTS-Mnt), 29 m^2/g (200-CTS-Mnt), 30 m^2/g (250-CTS-Mnt), 31 m^2/g (300-CTS-Mnt), and 36 m^2/g (350-CTS-Mnt) (Table 4), indicating that the CTS-Mnt can satisfy the adsorption sites required for the combination of CTS-Mnt and AFB_1 (illustrated in Fig. 8 ②, ③). At the same time, the experimental data were fitted with a linear isotherm adsorption model, and, with the increase in

Table 5 Fitted parameters of adsorption isotherms

AFB_1	Langmuir model			Freundlich model			Linear model	
	q_{max} (mg·g^{-1})	K_L	R^2	K_F	1/*n*	R^2	K_H	R^2
150-CTS-Mnt	3.64	1.83	0.9907	2.37	3.81	0.9455	0.50	0.9133
200-CTS-Mnt	4.03	2.06	0.9939	2.68	3.65	0.9631	0.66	0.9630
250-CTS-Mnt	4.73	3.14	0.9929	3.61	3.54	0.9583	1.10	0.9494
300-CTS-Mnt	4.83	6.08	0.9971	4.05	5.29	0.9779	1.05	0.9545
350-CTS-Mnt	4.97	16.64	0.9960	4.62	9.63	0.9771	1.23	0.9901

https://doi.org/10.1007/s42860-019-00042-z Published online by Cambridge University Press

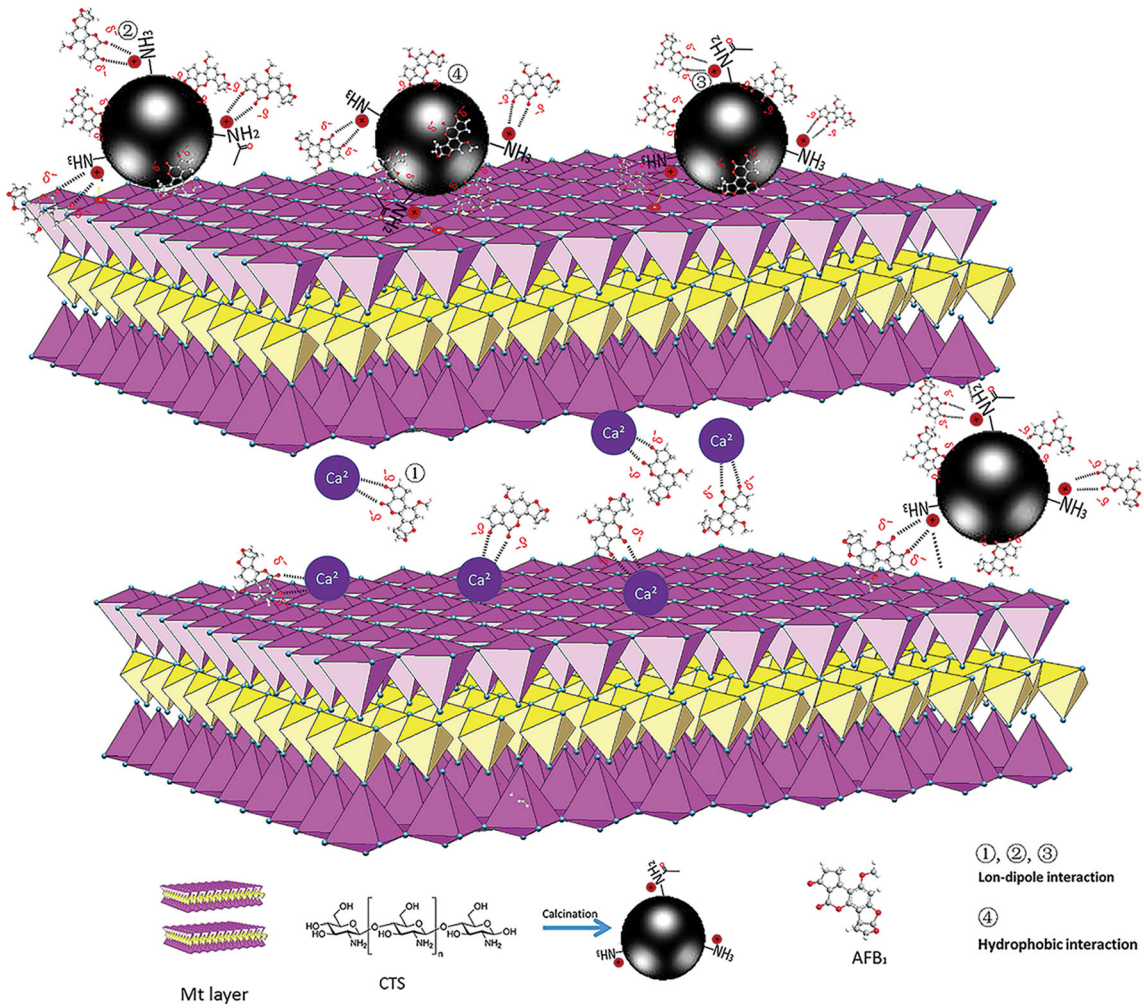

Fig. 8 Adsorption mechanisms of AFB_1 on 350-CTS-Mnt

calcination temperature, the adsorption of AFB_1 by CTS-Mnt clearly followed the trend of the linear isotherm adsorption model. When the calcination temperature was 350°C, 350-CTS-Mnt conformed better to the linear isotherm adsorption model (R^2 = 0.9901), indicating that hydrophobic interactions occurred in the adsorption process. In addition, its saturated adsorption capacity reached 4.97 mg/g^{-1}, which led to a better adsorption effect compared with other reported adsorbents (Table 6). As the calcination temperature increased, the deepening of carbonization of chitosan led to strong hydrophobicity (Fig. 4), which allowed the organic portion of AFB_1 to be adsorbed to the carbonized portion of the chitosan on the Mnt by hydrophobic interaction (Fig. 8 ④).

Table 6 Comparison of adsorption efficiency among the 350-CTS-Mnt and the most recently reported adsorbents of mycotoxin

Adsorbents	Mycotoxins	pH	Temp. (°C)	Adsorption Capacity (mg/g)	Reference
Mnt	AFB_1	3.5	37	0.51	this work
BS-12/Mts	AFB_1	3.5	37	4.21–4.58	(Wang et al. 2018)
LAB-35/Mts	AFB_1	3.5	37	4.47–4.65	(Wang et al. 2018)
Rectorite	AFB_1	3.5	37	3.25	(Sun et al. 2018)
Zeolite	AFB_1	-	30	0.81	(Marković et al. 2016a)
Octylphenolpolyoxyethylene ether	AFB_1	-	37	2.72	(Wang et al. 2018)
350-CTS-Mnt	AFB_1	3.5	37	4.97	This work

https://doi.org/10.1007/s42860-019-00042-z Published online by Cambridge University Press

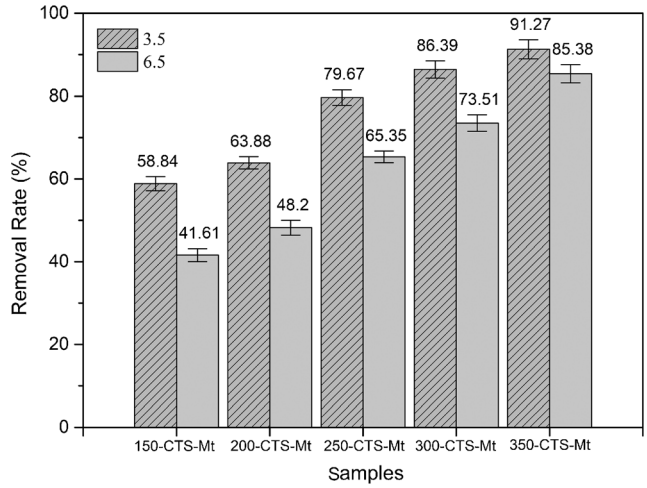

Fig. 9 Effect of pH on the adsorption performance of the heated CTS-Mnt for AFB_1. Initial concentration: 4 mg/L for AFB_1, adsorbent amount: 0.003 g.

Effect of pH

Normally, pH plays a key role in the mycotoxin adsorption process. The effects of pH 3.5 (pH of the stomach) and 6.5 (pH of the intestine) on the mycotoxin adsorbents are usually investigated. The adsorption experiments of five heated AFB_1 adsorbents (Fig. 9) were compared under these two pH conditions. The adsorption capacity under pH 3.5 is larger than that under pH 6.5, indicating that with increase in the pH of the adsorption environment from 3.5 to 6.5, some AFB_1 will be desorbed from the adsorbents. This may be due to the influence of pH on the cations in the Mnt layers (Wang et al. 2017). However, as the calcination temperature increased, the influence on the adsorption of AFB_1 of solution pH was inconspicuous. The possible reason is that the increase in the hydrophobicity of the adsorbents weakens the effect of pH on the cations in the Mnt layers.

CONCLUSIONS

In the present study, the effect of different calcination temperatures on CTS-Mnt was evaluated firstly by the detoxification of AFB_1. CTS-Mnt obtained at different calcination temperatures were characterized systematically and applied in the adsorption of AFB_1. The obvious findings are: stable CTS-Mnt was achieved at a calcination temperature of 350°C as CTS would be completely carbonized at 400°C. As the calcination temperature increased, the chitosan loaded on Mnt decomposed and carbonized gradually, which enhanced significantly the hydrophobicity of CTS-Mnt and the adsorption performance of CTS-Mnt for AFB_1 was improved significantly. When the calcination temperature was 350°C, the CTS-Mnt was relatively good hydrophobicity and a suitable chitosan loading so that 350-CTS-Mnt demonstrated the best adsorption performance for AFB_1. Furthermore, the adsorption of AFB_1 by CTS-Mnt is described mainly by the Langmuir isotherm adsorption model. Simultaneously, with the increase in calcination temperature, the hydrophobicity of CTS-Mnt increased, and the adsorption of AFB_1 by CTS-Mnt followed the trend of a linear isotherm adsorption model. When the calcination temperature reached 350°C, 350-CTS-Mnt can be described simultaneously using the Langmuir and linear isotherm adsorption models, and its saturated adsorption capacity reaches 4.97 mg/g^{-1}. These observations could indicate that 350-CTS-Mnt should be an ideal adsorbent in the mycotoxin removal field.

ACKNOWLEDGMENTS

The authors acknowledge gratefully the financial support provided by the National Natural Science Foundation of China (51774294), the Young Elite Scientists Sponsorship Program by CAST (2017QNRC001), the Yue Qi Young Scholar Project, China University of Mining & Technology (Beijing) and the Fundamental Research Funds for the Central Universities (2010YH10 and 2015QH01).

REFERENCES

Abbès, S., Salah-Abbès, J. B., Hetta, M. M., Ibrahim, M., Abdel-Wahhab, M. A., & Bacha, H. (2008). Efficacy of Tunisian montmorillonite for in vitro aflatoxin binding and in vivo amelioration of physiological alterations. *Applied Clay Science, 42*, 151–157.

Anjos, F. R. D., Ledoux, D. R., Rottinghaus, G. E., & Chimonyo, M. (2016). Efficacy of Mozambican bentonite and diatomaceous earth in reducing the toxic effects of aflatoxins in chicks. *World Mycotoxin Journal, 9*, 63–72.

Brunauer, S., Deming, L. S., Deming, W. E., & Teller, E. (1940). On a theory of the van der Waals adsorption of gases. *Journal of the American Chemical Society, 62*, 1723–1732.

Çelik, K., Uzatıcı, A., Coşkun, B., & Demir, E. (2013). Current developments in removal of mycotoxins by biological methods and chemical adsorbents. *Journal of Hygienic Engineering & Design*, 17–20.

Chen, L. I. (2016). Analysis of the clinical effect of montmorillonite powder combined with bifidobacterium tetravaccine in the treatment of children with allergic diarrhea. *Chinese Journal of the Frontiers of Medical Science, 2016(04)*. http://www.en.cnki.com.cn/Article_en/CJFDTotal-YXQY201604025.htm

Daković, A., Kragović, M., Rottinghaus, G. E., Ledoux, D. R., Butkeraitis, P., Vojislavljević, D. Z. Zarić, S.D., & Stamenić, L. (2012). Preparation and characterization of zinc-exchanged montmorillonite and its effectiveness as aflatoxin B_1 adsorbent. *Materials Chemistry and Physics, 137*, 213–220.

https://doi.org/10.1007/s42860-019-00042-z Published online by Cambridge University Press

del Pilar Monge, M., Magnoli, A. P., Bergesio, M. V., Tancredi, N., Magnoli, C. E., & Chiacchiera, S. M. (2016). Activated carbons as potentially useful non-nutritive additives to prevent the effect of fumonisin B_1 on sodium bentonite activity against chronic aflatoxicosis. *Food Additives & Contaminants, 33*, 10.

Hu, C., Deng, Y., Hu, H., Duan, Y., & Zhai, K. (2016). Adsorption and intercalation of low and medium molar mass chitosans on/in the sodium montmorillonite. *International Journal of Biological Macromolecules, 92*, 1191–1196.

Jackson, L. S., & Bullerman, L. B. (1999). Effect of processing on fusarium mycotoxins. *Oxygen Transport to Tissue XXXIII, 459*, 243–261.

Ji, C., Fan, Y., & Zhao, L. (2016). Review on biological degradation of mycotoxins. *Animal Nutrition, 2*(*03*), 5–11.

Katti, K. S., Katti, D. R., & Dash, R. (2008). Synthesis and characterization of a novel chitosan/montmorillonite/hydroxyapatite nanocomposite for bone tissue engineering. *Biomedical Materials, 3*(*3*), 034122.

Marković, M. A., Daković, A. S., Rottinghaus, G. E., Stojanović, M. D., Dondur, V. T., Kragović, M. M., & Zvonko, G. (2016a). Aflatoxin B_1 adsorption by the natural aluminosilicates – concentrate of montmorillonite and zeolite. *Hemijska Industrija, 70*, 519–524.

Marković, M., Daković, A., Rottinghaus, G. E., Kragović, M., Petković, A., Krajišnik, D., Milić, J., Mercurio, M., & de Gennaro, B. (2016b). Adsorption of the mycotoxin zearalenone by clinoptilolite and phillipsite zeolites treated with cetylpyridinium surfactant. *Colloids & Surfaces B Biointerfaces, 151*, 324.

Okolo, G. N., Everson, R. C., Neomagus, H. W. J. P., Roberts, M. J., & Sakurovs, R. J. F. (2015). Comparing the porosity and surface areas of coal as measured by gas adsorption, mercury intrusion and SAXS techniques. *Fuel, 141*, 293–304.

Park, Y., Ayoko, G. A., Horváth, E., Kurdi, R., Kristof, J., & Frost, R. L. (2013). Structural characterisation and environmental application of organoclays for the removal of phenolic compounds. *Journal of Colloid and Interface Science, 393*, 319–334.

Pereira, F. A. R., Sousa, K. S., Cavalcanti, G. R. S., Fonseca, M. G., De Souza, A. G., & Alves, A. P. M. (2013). Chitosan-montmorillonite biocomposite as an adsorbent for copper (II) cations from aqueous solutions. *International Journal of Biological Macromolecules, 61*, 471–478.

Phillips, T. D., Sarr, A. B., & Grant, P. G. (1995). Selective chemisorption and detoxification of aflatoxins by phyllosilicate clay. *Natural Toxins, 3*, 204–213 discussion 221.

Sun, Z., Ankang, S., Bin, W., Gaofeng, W., & Shuilin, Z. (2018). Adsorption behaviors of aflatoxin B_1, and zearalenone by organorectorite modified with quaternary ammonium salts. *Journal of Molecular Liquids, 264*, 645–651.

Taylor-Lange, S. C., Rajabali, F., Holsomback, N. A., Riding, K., & Juenger, M. C. G. (2014). The effect of zinc oxide additions on the performance of calcined sodium montmorillonite and illite shale supplementary cementitious materials. *Cement and Concrete Composites, 53*, 127–135.

Thimm, N., Schwaighofer, B., Ottner, F., Fröschl, H., Greifenender, S., & Binder, E. (2001). Adsorption of mycotoxins. *Mycotoxin Research, 17*, 219–223.

Wang, L., & Wang, A. Q. (2007). Removal of congo red from aqueous solution using a chitosan/organo-montmorillonite nanocomposite. *Journal of Chemical Technology & Biotechnology, 82*, 711–720.

Wang, L., & Wang, A. (2008). Adsorption properties of congo red from aqueous solution onto surfactant-modified montmorillonite. *Journal of Hazardous Materials, 160*, 173–180.

Wang, S. F., Shen, L., Tong, Y. J., Chen, L., Phang, I. Y., & Lim, P. Q. (2005). Biopolymer chitosan/montmorillonite nanocomposites: preparation and characterization. *Polymer Degradation and Stability, 90*, 123–131.

Wang, H., Tang, H., Liu, Z., Zhang, X., Hao, Z., & Liu, Z. (2014a). Removal of cobalt(II) ion from aqueous solution by chitosan–montmorillonite. *Journal of Environmental Sciences, 26*, 1879–1884.

Wang, X., Yang, L., Zhang, J., Wang, C., & Li, Q. (2014b). Preparation and characterization of chitosan–poly(vinyl alcohol)/bentonite nanocomposites for adsorption of Hg(II) ions. *Chemical Engineering Journal, 251*, 404–412.

Wang, G., Miao, Y., Sun, Z., & Zheng, S. (2017). Simultaneous adsorption of aflatoxin B_1 and zearalenone by mono- and di-alkyl cationic surfactants modified montmorillonites. *Journal of Colloid and Interface Science, 511*, 67–76.

Wang, G., Lian, C., Xi, Y., Sun, Z., & Zheng, S. (2018). Evaluation of nonionic surfactant modified montmorillonite as mycotoxins adsorbent for aflatoxin B_1, and zearalenone. *Journal of Colloid and Interface Science, 518*, 48–56.

Wang, G., Xi, Y., Lian, C., Sun, Z., & Zheng, S. (2019). Simultaneous detoxification of polar aflatoxin B_1 and weak polar zearalenone from simulated gastrointestinal tract by zwitterionic montmorillonites. *Journal of Hazardous Materials, 364*, 227–237.

Xu, J., Wang, L., & Zhu, Y. (2012). Decontamination of bisphenol A from aqueous solution by graphene adsorption. *Langmuir, 28*, 8418–8425.

Zhang, Y., Gao, R., Liu, M., Shi, B., Shan, A., & Cheng, B. (2015). Use of modified halloysite nanotubes in the feed reduces the toxic effects of zearalenone on sow reproduction and piglet development. *Theriogenology, 83*, 932–941.

Zhao, Z., Liu, N., Yang, L., Wang, J., Song, S., & Nie, D. (2015). Cross-linked chitosan polymers as generic adsorbents for simultaneous adsorption of multiple mycotoxins. *Food Control, 57*, 362–369.

Zhu, K., & Yao, R. (2014). Research progress on mycotoxins in food crop and its detection and removal methods. *Cereals & Oils, 2014*(*8*). http://en.cnki.com.cn/Article_en/CJFDTotal-LSYY201408018.htm

[*Received 15 January 2019; revised 26 October 2010; AE: Yael G. Mishael*]